Journal of Catalysis 281 (2011) 1–11

Contents lists available at ScienceDirect

Journal of Catalysis

journal homepage: www.elsevier.com/locate/jcat

# Microkinetic analysis and mechanism of the water gas shift reaction over copper catalysts

Rostam J. Madon [a,*], Drew Braden [b], Shampa Kandoi [b], Peter Nagel [a], Manos Mavrikakis [b], James A. Dumesic [b]

[a] BASF Corporation, 25 Middlesex-Essex Turnpike, Iselin, NJ 08830, United States
[b] Department of Chemical and Biological Engineering, University of Wisconsin, Madison, WI 53706, United States

ARTICLE INFO

*Article history:*
Received 19 October 2010
Revised 8 March 2011
Accepted 9 March 2011
Available online 6 May 2011

*Keywords:*
Water gas shift
Copper catalyst
Microkinetic modeling
Mechanism
Copper–zinc oxide–alumina

ABSTRACT

Using microkinetic modeling, we have determined the closed catalytic cycle that describes the water gas shift reaction on copper catalysts. Eight elementary reactions constitute the cycle. Dissociation of water and the recombination of surface hydrogen result in dihydrogen. While surface hydroxyl reacts with surface CO to give a surface carboxyl intermediate, which, in turn, reacts with another surface hydroxyl to give water and carbon dioxide to complete the cycle. The kinetic model further predicts that the most abundant surface species is a formate species formed via the hydrogenation of carbon dioxide. This reaction is not part of the catalytic cycle, and surface formate is a spectator species which increases substantially at high pressure and low temperature. Adsorption–desorption of dihydrogen is equilibrated; while water dissociation is kinetically significant with a high degree of irreversibility. And, depending on the reaction conditions, carboxyl formation also becomes kinetically important. The model identifies the binding energies of surface H, HCOO, and OH to be important parameters and allows us to explain the difference in the site time yields of various copper catalysts.



## 1. Introduction

Water gas shift is an important process step in the manufacture of ammonia, on-purpose hydrogen, and is used wherever CO needs to be converted to $CO_2$ with concurrent production of hydrogen. The reaction shown below is exothermic, and CO conversion is limited in commercial units by thermodynamic equilibrium.

$$CO + H_2O \rightleftarrows CO_2 + H_2 \quad \Delta H_{298K} = -41 \text{ kJ mol}^{-1}$$

Due to this limitation, commercially, the shift process is carried out in two steps: first, a high temperature water gas shift (HTS) step at 623–673 K over an iron-based catalyst, followed by a low temperature water gas shift (LTS) at 463–503 K over a Cu-based catalyst. The latter step brings CO levels below 0.5 mol%. This paper describes our attempts at understanding the reaction chemistry of LTS over commercially relevant $Cu–ZnO–Al_2O_3$ catalysts.

Since the introduction of the Cu catalyzed shift reaction over forty years ago, fundamental studies, both experimental and theoretical, have been carried out to understand this reaction. Since the early work of Yurieva [1] who proposed an associative mechanism and Grenoble et al. [2] who proposed a formic acid intermediate, investigations by Ovesen et al. [3,4], Campbell and co-workers [5–7], and Koryabkina et al. [8] exemplify the experimental approach used to elucidate the LTS mechanism. Recently, important theoretical studies [9–11] have added to our understanding of this reaction. But to date, the sequence of elementary steps that make up the LTS catalytic cycle remains unsettled. The debate centers around (a) a redox mechanism in which $O^*$ is formed either via a two-step water dissociation or $OH^*$ disproportionation, and then reacts with $CO^*$ to form $CO_2$ – where $*$ is an active site, and (b) a formate mechanism where $HCOO^*$ serves as a reactive intermediate [12,13]. Recently, Gokhale et al. [11] using a DFT (Density Functional Theory) investigation of the LTS reaction on Cu(1 1 1) proposed a new mechanism that involves a reactive surface carboxyl species, $^*COOH$.

The present study aims to resolve which elementary steps best describe the catalytic cycle for the Cu-catalyzed LTS reaction. Our analysis uses all proposed reaction steps that make chemical sense, as per DFT calculations, and employs the microkinetic approach described elsewhere [14]. With this approach, we obtain the steps that determine the LTS catalytic cycle as well as the kinetic parameters that describe these steps. Furthermore, this exercise identifies key parameters that affect LTS activity thus aiding experimental catalyst research. Importantly, by addressing these parameters either by altering catalyst components or by varying the preparation methodology, or both, one can obtain important insights into the LTS catalytic chemistry.

* Corresponding author. Fax: +1 732 205 5585.
*E-mail address:* rostam.madon@basf.com (R.J. Madon).

0021-9517/$ - see front matter © 2011 Elsevier Inc. All rights reserved.
doi:10.1016/j.jcat.2011.03.008

## 2. Experimental methods

### 2.1. Catalysts

The water gas shift catalysts studied here are composed of Cu, ZnO, and $Al_2O_3$. Traditionally, the catalyst is prepared [15,16] by coprecipitating the nitrates of Cu, Zn, and Al with sodium carbonate; at times sodium aluminate is also used. This precipitate is filtered, washed to remove sodium, dried, and calcined to decompose the carbonates. The catalyst may also be prepared with alumina powder [17,18]. Our standard precipitation takes place in 90 min at 333 K and at a constant pH of 7; the dried carbonate is calcined at 673 K until all carbonate is decomposed. Because these preparations are well known, we will not discuss them further. In the Results Section, as a particular catalyst is used in the model, we will note its composition and relevant properties.

### 2.2. Reactivity measurement

We carried out experimental reaction kinetics studies in a 12.7 mm OD fixed bed stainless steel reactor. We used 0.6 g of 0.3–0.15 mm (50–100 mesh) sized catalyst mixed with ca. 10 times the volume of similarly sized inert corundum powder to reduce temperature gradients. About 400 mm of the reactor above the catalyst bed acted as a preheater. Our control algorithm allowed us to maintain the average catalyst temperature at the set reaction temperature. We analyzed the reactor exit stream, including steam, with an online Agilent microGC.

Before reaction, we reduced the catalyst in dilute hydrogen taking precautions that there were no exotherms. The catalyst temperature was first raised to 443 K in He flowing at 500 $cm^3$(STP)/min. Three percent $H_2$ in He was introduced at the same flow rate; the concentration was then increased to 5% $H_2$ and finally to 20% $H_2$. The catalyst temperature was then raised over 1 h to 473 K in 20% $H_2$ in He, where it was kept for 2 h. The catalyst was flushed in $N_2$ before introducing reaction gases. Our *standard reaction conditions* were as follows: 2.7 bars absolute pressure, 473 K temperature, and an inlet feed composition of 36.7% $H_2$, 16.7% $N_2$, 8% CO, 5.3% $CO_2$, and 33.3% steam. The feed composition translated to a dry gas/steam molar ratio of 5. As we will see later, inclusion of product $CO_2$ in the inlet feed stream, as is practiced commercially, influences the modeling approach. Under these experimental conditions, the LTS reaction has a calculated equilibrium CO conversion of 98.6% [19]. For our modeling studies, we also used data obtained at other conditions: 30 bars total pressure, temperatures ranging from 453 to 503 K, as well as, inlet feed composition of 36.7% $H_2$, 16.7% $N_2$, 2.7% CO, 10.6% $CO_2$, and 33.3% steam. All experiments were carried out at a range of CO conversions obtained by varying catalyst weight-based gas hourly space-velocity (GHSV), wet basis. And in all experimental sets, conditions were repeated to ensure that there was no catalyst deactivation.

### 2.3. Cu dispersion measurement

We measured Cu dispersion (D) on fresh, reduced, catalyst samples using the $N_2O$ dissociative chemisorption method of Chinchen et al. [20] on a Micromeritics Autochem 2920. The chemisorption procedure involves bringing the reduced catalyst to 333 K in He, switching to 2% $N_2O$ in He, and monitoring the $N_2$ evolved with a calibrated thermal conductivity detector or with a mass spectrometer. For every dinitrogen evolved, one oxygen atom remains on the surface bonded to two surface Cu atoms. Using a Cu atom surface area of 0.68 $nm^2$ per atom obtained from a surface packing of $1.47 \times 10^{19}$ atoms $m^{-2}$, we calculate the percent dispersion (%D) and copper surface area. Assuming spherical particles, the relation, 1040/(%D), gives us Cu particle diameter in Å. *We thus report all reaction rates as site time yields*, Y $s^{-1}$.

## 3. Development of the microkinetic model

### 3.1. The reaction sequence

Table 1 shows 18 elementary steps that are suggested from results of DFT calculations [11] to describe the LTS reaction. They represent the various possible pathways: redox, formate-, and carboxyl-mediated mechanisms.

The first five reactions are common to all suggested mechanisms: adsorption of reactants and desorption of products plus the dissociation of steam. Reactions 6–8 describe the redox mechanism. Reactions 9–13 indicate a possible formate-mediated mechanism; Reaction 13 is important in that the bidentate formate is more stable than the monodentate intermediate. And although DFT analysis indicates that Reaction 12 is not an elementary step, we include it here since it has been suggested as a key reaction in the formate mechanism [5,12,13].

Finally, Reactions 14–18 represent the carboxyl mechanism. The carboxyl species forms as a cis configuration with the hydrogen of the hydroxyl pointing away from the surface [11]. This species transforms via Reaction 18 to the reactive trans species with hydrogen pointing toward the surface. The trans carboxyl may decompose (Reaction 15) and/or react with a surface hydroxyl species (Reaction 16) or with a surface O (Reaction 17) to give the product $CO_2$. Initially, we include all these steps in our model and allow microkinetic analysis to determine which steps constitute the LTS catalytic cycle.

### 3.2. Parameterization of the model

#### 3.2.1. Thermodynamic parameters

We parameterize the model in terms of *either* the forward or the reverse rate constant ($k_{i,for}$ or $k_{i,rev}$); these constants being related to the thermodynamic equilibrium constant ($K_{i,eq}$)

$$\frac{k_{i,for}}{k_{i,rev}} = K_{i,eq} \tag{1}$$

Therefore, we first calculate $K_{i,eq}$ for each of the 18 elementary steps of the reaction sequence. Since

$$K_{i,eq} = \exp\left(\frac{\Delta S_i^o}{R} - \frac{\Delta H_i^o}{RT}\right) \tag{2}$$

**Table 1**
Elementary steps used in the microkinetic modeling of LTS.

| Reaction step | Surface reactions |
|---|---|
| 1 | $CO + {}^* \leftrightarrow CO^*$ |
| 2 | $2H^* \leftrightarrow H_2 + 2^*$ |
| 3 | $H_2O + {}^* \leftrightarrow H_2O^*$ |
| 4 | $CO_2^* \leftrightarrow CO_2 + {}^*$ |
| 5 | $H_2O^* + {}^* \leftrightarrow H^* + OH^*$ |
| 6 | $OH^* + {}^* \leftrightarrow O^* + H^*$ |
| 7 | $CO^* + O^* \leftrightarrow CO_2^* + {}^*$ |
| 8 | $OH^* + OH^* \leftrightarrow H_2O^* + O^*$ |
| 9 | $CO_2^* + H^* \leftrightarrow HCOO^* + {}^*$ |
| 10 | $CO_2^* + H_2O^* \leftrightarrow HCOO^* + OH^*$ |
| 11 | $CO_2^* + OH^* \leftrightarrow HCOO^* + O^*$ |
| 12 | $CO^* + OH^* \leftrightarrow HCOO^* + {}^*$ |
| 13 | $HCOO^* + {}^* \leftrightarrow HCOO^{**}$ |
| 14 | $CO^* + OH^* \leftrightarrow COOH^*_{cis} + {}^*$ |
| 15 | $COOH^*_{trans} + {}^* \leftrightarrow CO_2^* + H^*$ |
| 16 | $COOH^*_{trans} + OH^* \leftrightarrow CO_2^* + H_2O^*$ |
| 17 | $COOH^* + O^* \leftrightarrow CO_2^* + OH^*$ |
| 18 | $COOH^*_{cis} \leftrightarrow COOH^*_{trans}$ |

we need to obtain standard entropy and enthalpy changes ($\Delta S_i^o$ and $\Delta H_i^o$) from the thermodynamic properties of all gaseous and surface species, with $R$ and $T$ being the gas constant and temperature, respectively.

First, we obtain or calculate the thermodynamic properties of all species in the gas phase. Calculations of gas phase entropies ($S_{gas}^o$), not available in handbooks, have been discussed in detail elsewhere [21,22]. We obtain gas phase enthalpies ($H_{gas}^o$), corrected for zero point energy (ZPE), from DFT calculations [11].

Next, we calculate the thermodynamic properties of all surface intermediates by relating them to the thermodynamic properties of gas phase species. We calculate the enthalpy of formation of a surface species, $H_{i,surface}^0$, as

$$H_{i,surface}^0 = H_{i,gas}^0 + BE_i + \Delta ZPE_i \quad (3)$$

where BE is the binding energy of an intermediate $i$ on Cu(1 1 1), and ΔZPE is the difference between the ZPE correction of the species on the surface and in the gas phase. Initial values of all BEs and all ZPEs are obtained from DFT calculations [11]. The BE is an important term that determines surface coverage of an intermediate.

Finally, the standard entropy for each surface intermediate is based on the local entropy of the corresponding gaseous species and is calculated as shown in Ref. [21]. The local entropy is obtained by subtracting the gaseous translational entropy from the standard entropy $S_{gas}^o$.

### 3.2.2. Kinetic parameters

For the adsorption–desorption steps 1–4, we define the rate constant in terms of adsorption, using collision theory to obtain the preexponential factor [14,23]. We then use the equilibrium constant to calculate the corresponding desorption rate constant. For surface reactions, we choose to define rate constants in the exothermic direction, where

$$k_i = A \exp\left(\frac{-E_i}{RT}\right) \quad (4)$$

$A$ is the preexponential factor, $E_i$ is the ZPE-corrected activation energy barrier in the exothermic direction. We obtain all preexponential factors via DFT calculations [11], and these are non-adjustable parameters in our model. Once the forward rate constant is obtained, we use the equilibrium constant to calculate the rate constant in the endothermic direction. We parameterize the kinetics of each surface step in terms of the ZPE-corrected activation energies.

Importantly, by basing the kinetic model on thermodynamic values for all reactants, intermediates, and observed products, and by using Eq. (1), we ensure that all kinetic parameters of the model are thermodynamically consistent.

## 3.3. Modeling approach

We use the microkinetic model to describe the experimentally measured CO conversions. The inputs to the model are the inlet flows of all gases, reaction temperature, total pressure, the total number of active sites in the reactor, and the experimentally determined CO conversions. Here, we assume that the active sites correspond to surface moles of Cu. We allow the reactor in the simulation to operate as a *transient* continuous stirred tank reactor (CSTR). We solve simultaneously 4 differential equations for the gaseous flow rates together with 10 differential equations for the fractional surface coverage of adsorbed intermediates, and one site balance equation. The solution then yields the four exit gas flow rates of $H_2$, CO, $CO_2$ and $H_2O$, the coverage of the 10 surface intermediates, and the forward and reverse rates and rate constants of all steps. The values of the fitted parameters are determined using the Athena Visual Studio engineering software [24] that has the solver and fitting routines built-in. The fitting procedure minimizes the sum of the squares of the residuals. The goodness of fit is derived by comparing predicted CO conversions obtained via the model and CO conversions via experimentation, and calculating the coefficient of determination, $R^2$, the value of which approaches unity as the fit improves.

Possible adjustable parameters in our model are the activation energies of the 18 steps given in Table 1, and the binding energies of the surface intermediates, except for the BEs of O and $COOH_{cis}$ which, as suggested in Ref. [11], are fixed. Activation energies of Reactions 1, 3, and 4 are all 0 kJ/mol since no bonds are broken. Thus, there are 23 possible adjustable parameters shown in Table 2 with the DFT-calculated values.

We make the initial parameter adjustments using a *transient* CSTR approach because the numerical methods used are robust when solving a series of simultaneous differential equations rather than a combination of algebraic and differential equations as one would solve in a plug flow reactor (PFR) or a CSTR operating at steady state. Robust numerical solving methods are necessary because errors inherent in DFT-predicted parameter values may lead to a poorly parameterized model and make converging on a solution difficult. A *transient* CSTR approach more easily adjusts the sensitive parameters from their DFT values.

Briefly, material balances for adsorbed species may be written as:

$$\frac{dS_i}{dt} = S_R Y_i \quad (5)$$

where $S_i$ is the number of molecules of species $i$ adsorbed on active catalyst sites, $S_R$ is the total number of active catalyst sites, and $Y_i$ is the site time yield per s for the formation of species $i$. Since for a *transient* CSTR $\frac{dS_i}{dt}$ is not zero, the differential equations for the adsorbed surface species and gas phase molecules are solved as a function of time during the simulation. The simulation starts with a vacant catalyst surface and a reactor charged with reactants and ends when the reactor reaches steady state operation, at which

**Table 2**
Binding energies and activation energies obtained from Ref. [11]and used as initial parameters for the model.

| | Parameters | From DFT |
|---|---|---|
| *Binding energy (kJ/mol)* | | |
| 1 | CO | 51.4 |
| 2 | H | 246.1 |
| 3 | $H_2O$ | 17.4 |
| 4 | $CO_2$ | 8.7 |
| 5 | OH | 275.0 |
| 6 | $COOH_{trans}$ | 181.4 |
| 7 | HCOO (monodentate) | 223.9 |
| 8 | HCOO (bidentate) | 267.3 |
| *Activation energy (kJ/mol)* | | |
| 9 | $H_2 + 2^* \leftrightarrow 2H^*$ | 52.1 |
| 10 | $H_2O^* + ^* \leftrightarrow H^* + OH^*$ | 131.2 |
| 11 | $OH^* + ^* \leftrightarrow O^* + H^*$ | 169.8 |
| 12 | $CO^* + O^* \leftrightarrow CO_2^* + ^*$ | 79.0 |
| 13 | $CO^* + OH^* \leftrightarrow COOH_{cis}^* + ^*$ | 58.9 |
| 14 | $COOH_{trans}^* + ^* \leftrightarrow CO_2^* + H^*$ | 136.0 |
| 15 | $COOH_{trans}^* + OH^* \leftrightarrow CO_2^* + H_2O^*$ | 40.5 |
| 16 | $CO^* + OH^* \leftrightarrow HCOO^* + ^*$ | 300.0 |
| 17 | $CO_2^* + H^* \leftrightarrow HCOO^* + ^*$ | 71.4 |
| 18 | $CO_2^* + H_2O^* \leftrightarrow HCOO^* + OH^*$ | 260.0 |
| 19 | $OH^* + OH^* \leftrightarrow H_2O^* + O^*$ | 0.0 |
| 20 | $CO_2^* + OH^* \leftrightarrow HCOO^* + O^*$ | 132.0 |
| 21 | $COOH^* + O^* \leftrightarrow CO_2^* + OH^*$ | 60.0 |
| 22 | $HCOO^* + ^* \leftrightarrow HCOO^{**}$ | 9.7 |
| 23 | $COOH_{cis}^* \leftrightarrow COOH_{trans}^*$ | 50.2 |

point $\frac{dS_i}{dt}$ equals zero; i.e., the composition of the reactor effluent and the catalyst surface coverage are constant with time, as required in a CSTR operating at steady state.

Material balances for gaseous species may be written as:

$$\frac{dF_i^{out}}{dt} = K_{void}\left[F_i^{in} - F_i^{out} + S_R Y_i\right] \quad (6)$$

where $F_i^{out}$ and $F_i^{in}$ are the outlet and inlet molar flow rates of species *i*. The constant $K_{void}$ depends on the amount of void space in the reactor, and its value is taken to be unity. (This value only scales the length of the transient, and it does not alter the steady state performance of the reactor.)

We begin modeling with parameter values shown in Table 2. The model adjusts the sensitive parameters, as a good fit is found for the input data, at a given set of experimental conditions. This new set of parameters then describes the kinetics of the LTS reaction. For the model to be realistic and robust, the parameter set should describe the LTS reaction over a range of conditions. Importantly, parameters obtained using a *transient* CSTR approach serve as good initial values for simulations using the PFR approach.

Material balances for surface and gaseous species may be written as follows for the PFR approach:

$$\frac{dS_i}{dt} = 0 \quad (7)$$

$$\frac{dF_i}{dS} = Y_i \quad (8)$$

where *S* is the number of surface sites, equal to zero at the reactor inlet and $S_R$ at the exit.

However, elucidation and description of reaction kinetics phenomena in terms of catalyst properties are most clearly accomplished in a CSTR compared to a PFR, because all of the catalyst in a CSTR operates at the same well-mixed composition of reactants and products. Whereas a gradient of compositions exists in a PFR and the catalyst bed operates in this non-uniform environment. Therefore, discussions of how surface coverages on the catalyst are affected by the presence of promoters or by changes in binding energies of intermediates on the catalyst are clearer when the catalyst is simulated in a CSTR compared to a PFR. Therefore we have used a CSTR to probe such effects.

Errors associated with experimental work and with solver operation may result in small variations in key parameters; we, *ad hoc*, allow variations in such parameters by ±4 kJ/mol as experimental conditions and catalysts are changed. However, we will address variations for any key parameter as the need arises. Errors associated with DFT calculations for binding and activation energies are about ±10 kJ/mol.

Importantly, we determined that when starting within the above acceptable DFT error limit, the same optimal parameter fits were obtained. Thus, our study accurately captured the most probable solution when we initialized within the acceptable DFT confidence limits. Moreover, as shown later, our conclusions regarding the reaction pathway for the water gas shift reaction did not change even when we moved the parameters from DFT values by much larger amounts.

## 4. Results

Before we describe our results and discuss the chemistry of the LTS reaction, we need to show that the kinetic data are free from transport artifacts. To that end, we made two catalysts ensuring all preparative parameters were identical except for the Cu and ZnO amounts, thus allowing us to change the Cu surface area by about a factor of two. The first catalyst contained 46% Cu, 31% ZnO, 23% $Al_2O_3$, Cu dispersion of 6.2%, and Cu surface area of 18.4 $m^2/g$. And the second catalyst contained 21% Cu, 55% ZnO, 24% $Al_2O_3$, Cu dispersion of 7.1%, and Cu surface area of 9.7 $m^2/g$. At the standard experimental conditions, and 40% CO conversion, the reaction rates were 0.13 and 0.12 $s^{-1}$, respectively. In accord with the criterion discussed elsewhere [25,26], this identity of rates for catalysts with the number of surface sites differing by about a factor of two ensures that kinetic data are free from heat and mass transfer limitations as well as catalyst by-passing and poisoning.

### 4.1. The microkinetic model and catalytic cycle for the LTS reaction

We obtained all data, in this section, using a catalyst containing 52% Cu, 32% ZnO, 16% $Al_2O_3$, with a Cu dispersion of 4.5%. First, to obtain the catalytic cycle, we used our standard reaction conditions and modeled CO conversion – GHSV results using the parameters in Table 2 as our initial input. Fig. 1 shows the result of the simulation as a parity plot ($R^2$ = 0.987), and Table 3 shows changes in the initial parameter set to achieve the result. Remarkably, almost all our initial input parameters remain unchanged: there are minor changes for the BEs of H, OH, and bidentate HCOO, a 6 kJ/mol and a 10 kJ/mol change in the activation energies of steam dissociation and $COOH^*_{cis}$ formation, respectively. The simulation further demonstrates (Fig. 2) that the model predicts reaction rates very well. Accordingly, we can now use these predictions to find which elementary reactions constitute the closed catalytic cycle and which reactions do not play a role in LTS chemistry.

Table 4 gives the net rates derived by the model for of all the reactions at 25% CO conversion. Although comparison at any conversion is valid, it is always useful to compare far from the overall

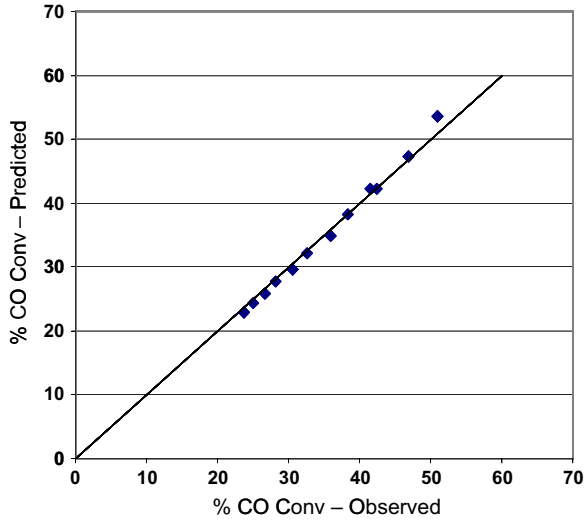


**Fig. 1.** Simulation results at standard reaction conditions: parity plot for % CO conversion.

**Table 3**
Model derived parameter changes at standard reaction conditions.

| Parameters | DFT (kJ/mol) | Model (kJ/mol) |
|---|---|---|
| *All binding energies same as DFT values EXCEPT* | | |
| $BE_H$ | 246.1 | 245.1 |
| $BE_{OH}$ | 275 | 276.3 |
| $BE_{HCOO}$ (bidentate) | 267.3 | 265.1 |
| *All activation energies same as DFT values EXCEPT* | | |
| $E_5$ $H_2O^* + * \leftrightarrow H^* + OH^*$ | 131.2 | 125 |
| $E_{14}$ $CO^* + OH^* \leftrightarrow COOH^*_{cis} + *$ | 58.9 | 48.7 |

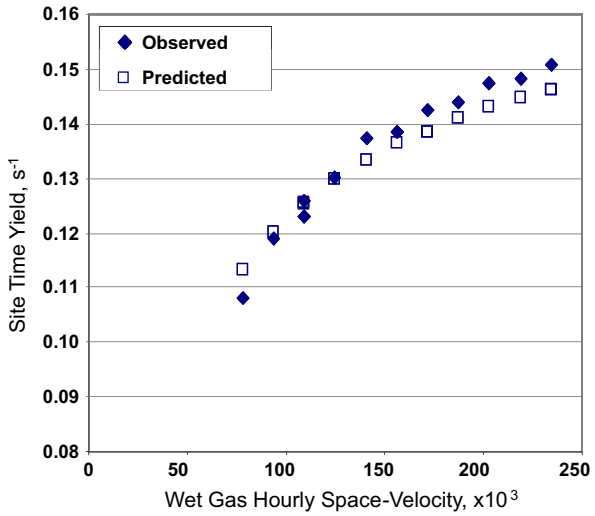


**Fig. 2.** Simulation results for site time yields, standard reaction conditions.

**Table 4**
Net rates of elementary steps at standard reaction conditions, 25% CO conversion.

| Surface reactions | | Net rates ($s^{-1}$) |
|---|---|---|
| 1. | $CO + * \leftrightarrow CO^*$ | 0.145 |
| 2. | $2H^* \leftrightarrow H_2 + 2^*$ | 0.145 |
| 3. | $H_2O + * \leftrightarrow H_2O^*$ | 0.145 |
| 4. | $CO_2^* \leftrightarrow CO_2 + *$ | 0.145 |
| 5. | $H_2O^* + * \leftrightarrow H^* + OH^*$ | 0.290 |
| 6. | $OH^* + * \leftrightarrow O^* + H^*$ | $10^{-17}$ |
| 7. | $CO^* + O^* \leftrightarrow CO_2^* + *$ | $10^{-10}$ |
| 8. | $OH^* + OH^* \leftrightarrow H_2O^* + O^*$ | $10^{-10}$ |
| 9. | $CO_2^* + H^* \leftrightarrow HCOO^* + *$ | $10^{-17}$ |
| 10. | $CO_2^* + H_2O^* \leftrightarrow HCOO^* + OH^*$ | $10^{-26}$ |
| 11. | $CO_2^* + OH^* \leftrightarrow HCOO^* + O^*$ | $10^{-17}$ |
| 12. | $CO^* + OH^* \leftrightarrow HCOO^* + *$ | $10^{-28}$ |
| 13. | $HCOO^* + * \leftrightarrow HCOO^{**}$ | $10^{-8}$ |
| 14. | $CO^* + OH^* \leftrightarrow COOH^*_{cis} + *$ | 0.145 |
| 15. | $COOH^*_{trans} + ** \leftrightarrow CO_2^* + H^*$ | $10^{-6}$ |
| 16. | $COOH^*_{trans} + OH^* \leftrightarrow CO_2^* + H_2O^*$ | 0.145 |
| 17. | $COOH^* + O^* \leftrightarrow CO_2^* + OH^*$ | $10^{-11}$ |
| 18. | $COOH^*_{cis} \leftrightarrow COOH^*_{trans}$ | 0.145 |

thermodynamic equilibrium conversion of 98.6%. The experimental rate at 25% CO conversion is 0.148 $s^{-1}$. Since net rates of all reactions in a catalytic cycle must be the same as the overall rate of reaction, after correction for the stoichiometric number of a step, Table 4 identifies the reaction steps that constitute the catalytic cycle for the LTS reaction. Reactions 1–5, 14, 16, and 18 have the same net rate as the overall experimentally observed value. Reaction 5, the dissociation of water, has a stoichiometric number of 2; i.e., two water molecules are dissociated in a cycle. And, although the carboxyl intermediate can react via steps 15–17 to give the product $CO_2$, the model indicates that step 16 is the relevant step in the mechanism.

Reaction 7, the reaction of $CO^*$ with $O^*$, and Reaction 8, the disproportionation of surface hydroxyls, key reactions in the redox mechanism, have very low rates of $10^{-10}$ $s^{-1}$. Importantly, even, in a what-if simulation, when we force the activation energy of step 7 from a DFT-calculated value of 79 to 10 kJ/mol, the net rate of $CO^*$ oxidation is still an order of magnitude lower than the experimental value. Furthermore, all steps containing the formate intermediate also have extremely low net rates. Thus steps associated with the redox mechanism or formate-mediated mechanism are not part of the LTS cycle.

The sequence of elementary steps that describe the reaction mechanism for LTS on Cu is given in Table 5. The ratio of forward/reverse rates indicates that Reactions 1–4 and 18 are in quasi-equilibrium. The ratio of net rate/forward rate ($\delta$) gives the degree of irreversibility or distance from equilibrium; as $\delta \to 0$, the reaction approaches equilibrium; and as $\delta \to 1$, the reaction becomes irreversible. As noted by Boudart [27] in terms of the chemical affinity $A_F$

$$\delta = 1 - \exp\left(-\frac{A_F}{RT}\right) \tag{9}$$

This ratio $\delta$ for step 5 is 0.88; thus, steam dissociation is the most irreversible step in the sequence. Steps 14 and 16 are reversible but not in quasi-equilibrium.

We next address another important result from the model that bidentate formate is the most abundant surface species. The mechanism given in Table 5 does not account for surface formate species that have also been discussed elsewhere [4,5,12,13]. Therefore we need to identify which of the five reactions that involve surface formate participate in the surface chemistry, albeit not as part of the LTS catalytic cycle. As noted in Table 4, these reactions have very low net rates. Reactions 10–12 also have extremely low forward rates (Table 6), whereas Reactions 9 and 13 have higher forward and reverse rates and are in quasi-equilibrium. Steps 9 and 13 adequately describe the formation of the bidentate formate intermediate; the formate intermediate is not involved in the LTS reaction directly and is a spectator species that affects the LTS reaction by its surface coverage in accord with Refs. [4,11].

### 4.1.3. Model at varying pressure and temperature

Henceforth, we omit all unimportant reactions from the fitting process and fit all data with only Reactions 1–5, 9, 13, 14, 16, 18, and with the germane, reduced parameter set.

Using the same catalyst and the same reactant gas mixture as above, we obtained data at 2.7 and 30 bars at 473 K, and over a temperature range from 453 to 503 K at 2.7 bars. Figs. 3 and 4 show the parity plots for CO conversion for the pressure and temperature sets, respectively, over a wide range of conversions. We obtained excellent fits, $R^2 = 0.983$ for the pressure set and $R^2 = 0.984$ for the temperature set, with the *same* model parameters (Table 3) without any adjustment. This agreement substanti-

**Table 5**
The catalytic cycle for LTS on copper.

| The LTS mechanism | | Forward/reverse rate | Net/forward rate ($\delta$) |
|---|---|---|---|
| 1. | $CO + * \leftrightarrow CO^*$ | 1.0 | $10^{-7}$ |
| 2. | $2H^* \leftrightarrow H_2 + 2^*$ | 1.0 | $10^{-4}$ |
| 3. | $H_2O + * \leftrightarrow H_2O^*$ | 1.0 | $10^{-8}$ |
| 4. | $CO_2^* \leftrightarrow CO_2 + *$ | 1.0 | $10^{-7}$ |
| 5. | $2H_2O^* + 2^* \leftrightarrow 2H^* + 2OH^*$ | 8.3 | 0.88 |
| 14. | $CO^* + OH^* \leftrightarrow COOH^*_{cis} + *$ | 2.2 | 0.54 |
| 16. | $COOH^*_{trans} + OH^* \leftrightarrow CO_2^* + H_2O^*$ | 1.1 | 0.06 |
| 18. | $COOH^*_{cis} \leftrightarrow COOH^*_{trans}$ | 1.0 | $10^{-3}$ |
| | $CO + H_2O \leftrightarrow CO_2 + H_2$ | | |

**Table 6**
Forward reaction rates for formate-producing reactions (25% CO conversion).

| Formate reactions | | Forward rate, $s^{-1}$ |
|---|---|---|
| 9. | $CO_2^* + H^* \leftrightarrow HCOO^* + *$ | $10^{-3}$ |
| 10. | $CO_2^* + H_2O^* \leftrightarrow HCOO^* + OH^*$ | $10^{-27}$ |
| 11. | $CO_2^* + OH^* \leftrightarrow HCOO^* + O^*$ | $10^{-18}$ |
| 12. | $CO^* + OH^* \leftrightarrow HCOO^* + *$ | $10^{-28}$ |
| 13. | $HCOO^* + * \leftrightarrow HCOO^{**}$ | $10^{+7}$ |

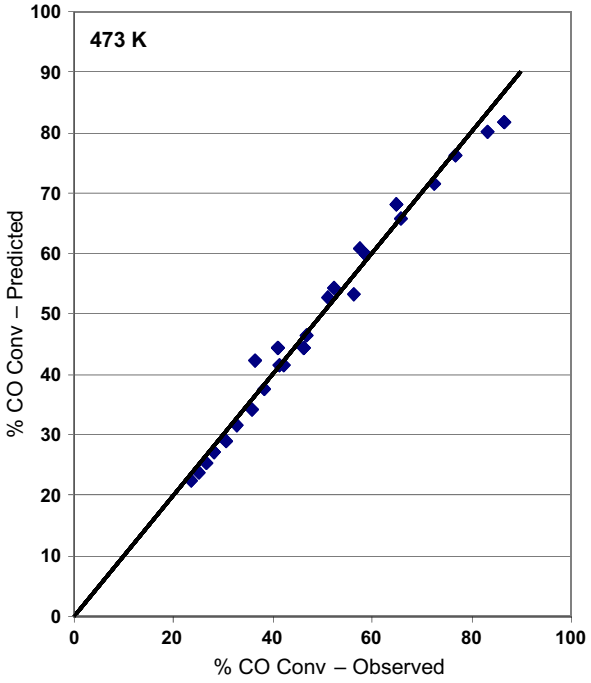


**Fig. 3.** Simulation results at 2.7 and 30 bars pressure, 473 K, feed composition: 36.7% $H_2$, 16.7% $N_2$, 8% CO, 5.3% $CO_2$, 33.3% steam.

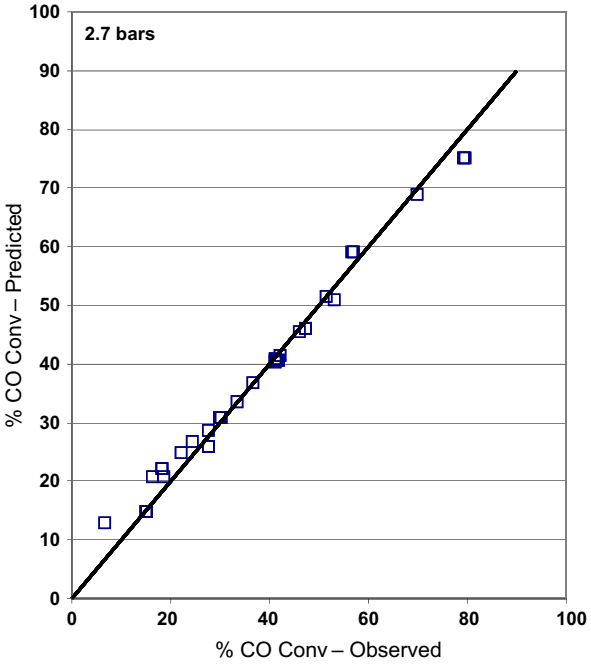


**Fig. 4.** Simulation results for a temperature range of 453–503 K, 2.7 bars, feed composition: 36.7% $H_2$, 16.7% $N_2$, 8% CO, 5.3% $CO_2$, 33.3% steam.

ates the validity of the mechanism over a wide range of temperatures and pressures. The excellent fit over a 50 K temperature range confirms that the activation energies obtained from both the DFT calculations and the model are accurate. And the arguments of reaction equilibrium and reversibility remain unchanged.

Experimentally, we obtained an overall apparent activation energy of 73 kJ/mol calculated at ca. 30% CO conversion and a temperature range from 458 to 498 K. This value is close to the activation energy of 79 kJ/mol obtained by Koryabkina et al. [8], using a commercial Cu:ZnO:$Al_2O_3$ catalyst and experimental conditions close to ours. Although we did not obtain reaction orders for individual components, the near identity of site time yields at 2.7 and 30 bars pressure indicates a near zero-order dependence on pressure, similar to the observations in Ref. [8].

*4.1.4. Surface coverage*

Fig. 5 shows surface coverages at 2.7 and 30 bars pressure. At the lower pressure, the coverage is low with 8–10% $HCOO^{**}$, 2% $H^*$, and 0.5% $CO^*$. The rest of the surface species, including the important intermediate $COOH^*_{trans}$, have a fractional coverage of $10^{-5}$ or less. At higher pressure, there is a significant increase in bidentate formate coverage, a small increase in $CO^*$ and no change in $H^*$. Fig. 6 shows the effect of temperature on coverage at 27% CO conversion. There is a significant decrease in $HCOO^{**}$ as temperature increases, with no concurrent change in H coverage. Neither temperature nor pressure alters coverage of other intermediates to any determinant degree; only formate determines to what extent the reactive surface is crowded or not.

*4.1.5. Plug flow analysis*

So far we have generated a robust parameter set and obtained all model results using the *transient* CSTR approach. With

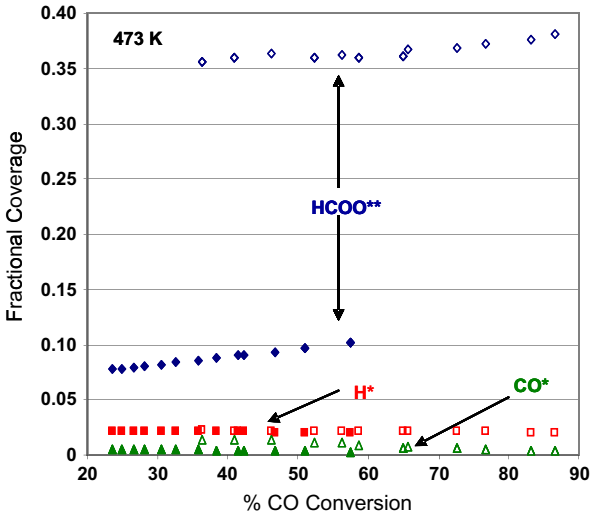


**Fig. 5.** Surface coverage at 2.7 (closed points) and 30 bars (open points) pressure, 473 K, feed composition: 36.7% $H_2$, 16.7% $N_2$, 8% CO, 5.3% $CO_2$, 33.3% steam.

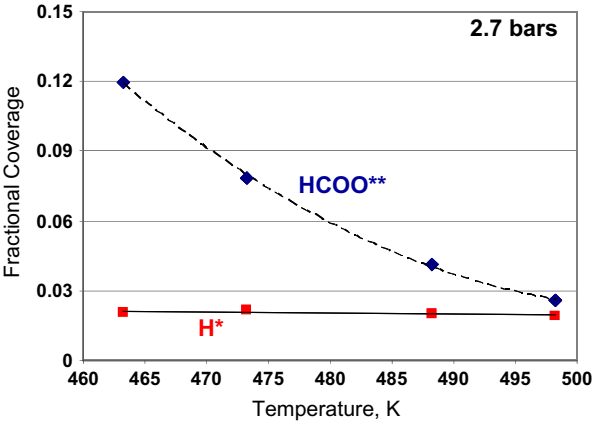


**Fig. 6.** Formate and hydrogen coverage versus temperature, 2.7 bars total pressure, feed composition: 36.7% $H_2$, 16.7% $N_2$, 8% CO, 5.3% $CO_2$, 33.3% steam.

these parameters, we now fit the combined data of Figs. 3 and 4 using the PFR approach. We obtain an excellent fit (Fig. 7) of all the data at two pressures and various temperatures with minimal changes of 3 kJ/mol or less for $BE_H$, $BE_{HCOO}$, and $BE_{OH}$. Fig. 8 shows the surface coverage for HCOO** and $H^*$. CSTR analysis gives surface coverage throughout the well-mixed reactor, whereas, for the PFR, we plot coverage at the exit of the reactor. The predicted results between CSTR and PFR approaches are remarkably consistent and give credence to the robustness of the model. Such consistency is expected in reactions where there is modest inhibition of the rate by product species that are not present in the feed stream. In our case, co-feeding $CO_2$ at reactor inlet ensures formation of bidentate formate throughout the PFR, thus allowing facile transition from the CSTR approach to a PFR approach. Furthermore, as noted earlier, the overall pressure dependence for the LTS reaction is close to zero.

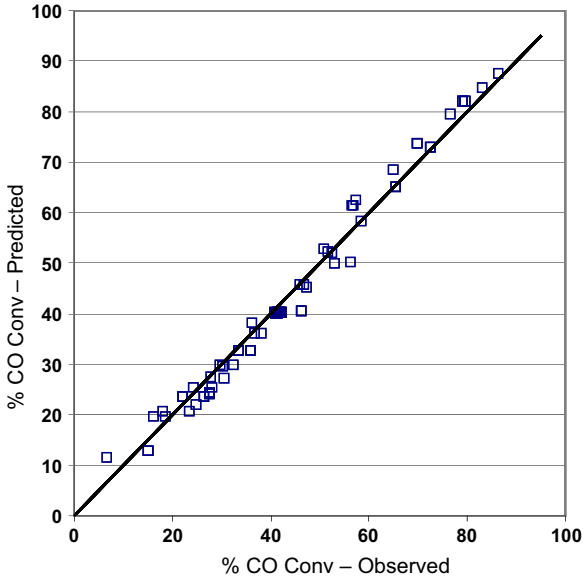


**Fig. 7.** Simulation results using plug flow analysis with combined data from Figs. 4 and 5.

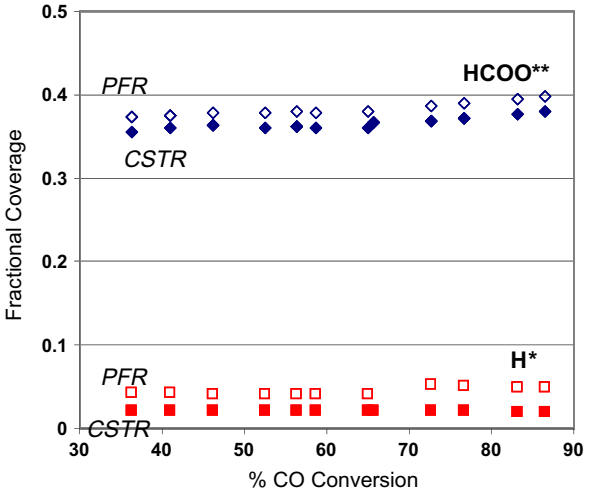


**Fig. 8.** Formate and hydrogen coverage using transient CSTR (closed points) and plug flow (open points) analyses at 30 bars total pressure, 473 K, feed composition: 36.7% $H_2$, 16.7% $N_2$, 8% CO, 5.3% $CO_2$, 33.3% steam.

#### 4.1.6. Variation in CO and $CO_2$ levels

Here, we study the LTS reaction at 2.7 bars pressure, temperature ranging from 458 to 488 K, and inlet feed composition of 36.7% $H_2$, 16.7% $N_2$, 2.7% CO, 10.6% $CO_2$, and 33.3% steam. Compared to our standard conditions, we change the $CO/CO_2$ ratio from 1.5 to 0.25. This low $CO/CO_2$ ratio mimics commercial values for example in ammonia synthesis plants. We obtain (Fig. 9) an excellent fit for 64 data at four different temperatures, $R^2 = 0.982$, using the same parameter set as in Table 3 with a minimal increase of 3 kJ/mol for $BE_H$ and a decrease of 6 kJ/mol for $BE_{OH}$. At the lower $CO/CO_2$ ratio, the reaction rate decreases significantly; Fig. 10, at 473 K and 2.7 bars, demonstrates how well the model describes this change in rates.

### 4.2. Modeling changes in LTS catalyst

#### 4.2.1. Alkali as promoter

Our model indicates that bidentate formate is not only the most abundant surface species but that it increases significantly with increasing pressure and decreasing temperature. This result is important since bidentate formate has been suggested [4,28] to be an intermediate during methanol formation over Cu.

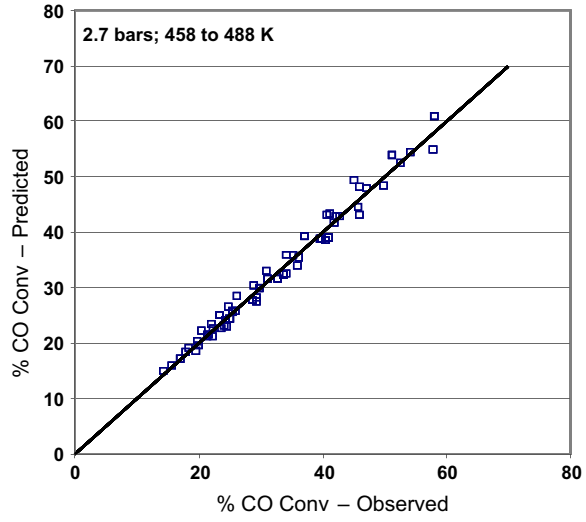


**Fig. 9.** Simulation results for a temperature range of 458–488 K, 2.7 bars total pressure, feed composition: 36.7% $H_2$, 16.7% $N_2$, 2.7% CO, 10.6% $CO_2$, 33.3% steam.

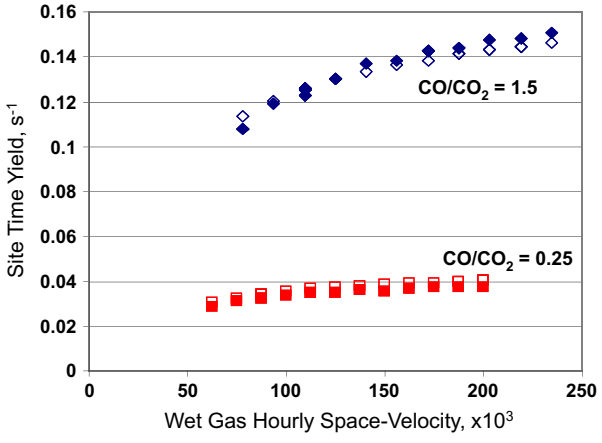


**Fig. 10.** Site time yield comparisons. Experimental – closed symbols, model – open symbols. Pressure 2.7 bars, Temperature 473 K. Diamond symbol: 36.7% $H_2$, 16.7% $N_2$, 8% CO, 5.3% $CO_2$, 33.3% steam. Square symbols: 36.7% $H_2$, 16.7% $N_2$, 2.7% CO, 10.6% $CO_2$, 33.3% steam.

Methanol, even in ppm levels, is an unwanted byproduct during commercial LTS operation and is particularly prevalent at high pressures used commercially. However, addition of alkali to the Cu catalyst [18,29] mitigates methanol formation. We therefore used a catalyst containing 49% Cu, 33% ZnO, 17% $Al_2O_3$, and 1% $K_2O$ plus $Cs_2O$, Cu dispersion of 4.5%, for LTS at 30 bars pressure, 473 K, and standard feed composition to obtain %CO conversion versus GHSV data. We were unable to model these data with parameters from Table 3. Only after the value of $BE_H$ was reduced from −245 kJ/mol to −234 kJ/mol and the value of $BE_{HCOO}$ was reduced from −265 kJ/mol to −220 kJ/mol, were we able to obtain an excellent fit with $R^2 = 0.963$. These changes resulted in a small decrease in H coverage from 2% to 0.5% and a substantial decrease in HCOO** from 36% to 0.005%. Thus, the presence of alkali appears to destabilize the formation of bidentate formate, and we infer that the reduction in methanol formation is due to such destabilization of a key intermediate. The model teaches us that formate species in LTS is not only a spectator species, but it probably plays a role in byproduct methanol formation. However, we were unable to observe ppm levels of methanol, so the connection between formate intermediate and methanol product is by analogy with previous work.

*4.2.2. Varying catalyst site time yield*

In the previous section, we varied the reaction rate by changing the $CO/CO_2$ ratio, and the model was able to describe the data well. Here, we investigate four catalysts with varying activities. Table 7 gives catalyst composition, Cu dispersion, and site time yields at ca. 35% CO conversion. Catalysts 1 and 2 are from a single batch of catalyst made with our standard method as noted in Section 2.1. We calcined Catalyst 1 at 673 K for 2 h to completely decompose the carbonate, whereas Catalyst 2 was calcined at a lower temperature, 523 K for 2 h, and a substantial amount of carbonate remained before the catalyst was reduced. We made Catalysts 3 and 4 in the same way as Catalyst 1, except that neodymium nitrate was added to the copper and zinc nitrate before precipitation for Catalyst 3, and yttrium nitrate was used for Catalyst 4.

Fig. 11 shows the model description of the rate data for all four catalysts. Remarkably, the model describes the data for all catalysts with only one parameter, $BE_H$, needing to be changed for each catalyst as shown in Fig. 12. The systematic decrease in $BE_H$ from −249 kJ/mol for the most active catalyst to −241 kJ/mol for the least active catalyst suggests that $BE_H$ is a key sensitive parameter that defines surface behavior during LTS. Fig. 13 shows a systematic decrease in H* coverage as catalyst activity decreases; HCOO** and CO* coverages remain invariant with catalyst activity.

*4.3. Sensitivity analysis*

Here, we use Campbell's formalism for the degree of rate control [30], where the degree of rate control $X_{RC,i}$ for an elementary step $i$ is defined as

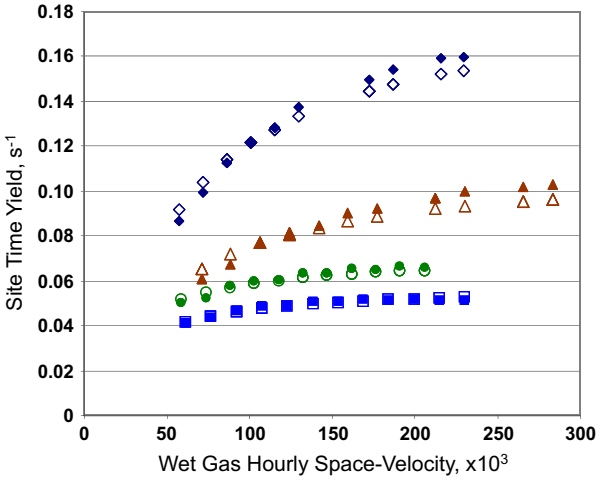


**Fig. 11.** Site time yield comparisons for Catalysts 1–4 (Table 7). Experimental – closed symbols, Model – open symbols. Standard reaction conditions.

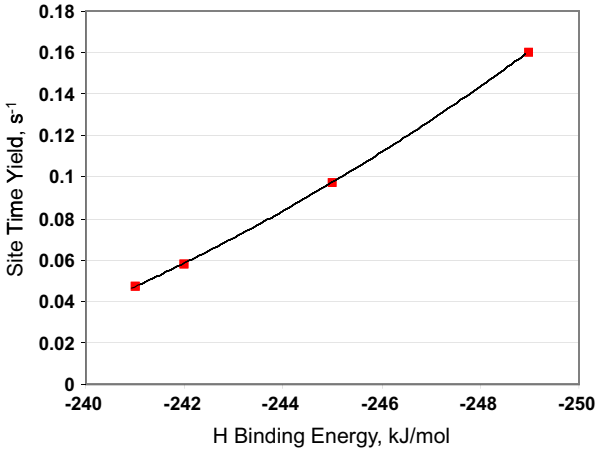


**Fig. 12.** Model prediction: systematic decrease in H binding energy as activity decreases for Catalysts 1–4 (Table 7) at 35% CO conversion. Standard reaction conditions.

$$X_{RC,i} = \frac{k_i}{Y}\left(\frac{\delta Y}{\delta k_i}\right)_{K_{i,eq},k_{j\neq i}} \tag{10}$$

where $k_i$ is the rate constant for step $i$, $K_{i,eq}$ is the equilibrium constant for this step, and $Y$ is the rate of the overall reaction. Thus, we calculate $X_{RC,i}$ for each step $i$ by computing the effect on the net rate $Y$ of increasing the forward and reverse rate constants for a given step $i$ while maintaining $K_{i,eq}$ and $k$ for all other steps constant. For all equilibrated steps, $X_{RC,i}$ is 0. Table 8 gives $X_{RC,i}$ at 25% CO conversion for steps 5, 14, and 16 at our standard conditions, and at the condition where the $CO/CO_2$ ratio was changed from 1.5 to 0.25. At the standard conditions, $X_{RC,5}$ is 0.79 while the other non-equilibrated steps have much lower values. These values are directionally the same as the degree of irreversibility given in Table 5. However, when we change the molar composition of CO and $CO_2$, $X_{RC,5}$ decreases to 0.6 while $X_{RC,14}$ increases to 0.2, indicating that the kinetic importance of step 14 has increased. Interestingly, Table 8 shows that $\sum_i X_{RC,i} \neq 1$. We explore this further in Fig. 14, where $\sum_i X_{RC,i}$ is plotted versus %CO conversion. $\sum_i X_{RC,i} = 1$ only as conversion tends to zero.

Recently, Stegelmann et al. [31] evaluated the degree of thermodynamic control of surface intermediates, thus examining how stabilization of surface intermediates affected reaction rates.

**Table 7**
Catalyst compositions, Cu dispersions, and site time yields at standard reaction conditions.

| Catalyst | Cu (wt%) | ZnO (wt%) | $Al_2O_3$ (wt%) | Additive (wt%) | Cu dispersion (%) | Y at 35% CO conversion ($s^{-1}$) |
|---|---|---|---|---|---|---|
| 1 | 46 | 29 | 25 | – | 10 | 0.16 |
| 2 | 46 | 29 | 25 | – | 7 | 0.097 |
| 3 | 45 | 24 | 26 | $Nd_2O_3$ = 5 | 8 | 0.058 |
| 4 | 45 | 24 | 26 | $Y_2O_3$ = 5 | 10 | 0.047 |

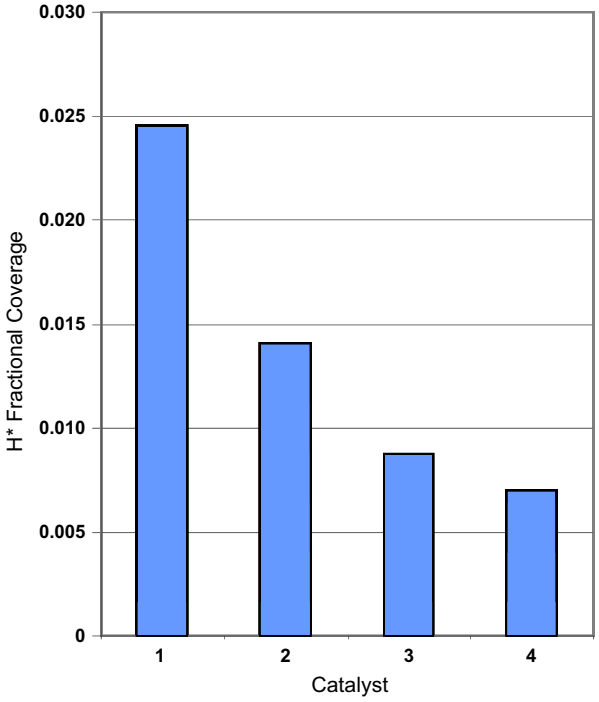


**Fig. 13.** Model prediction: surface H coverage decreases as activity decreases for Catalysts 1–4 (Table 7) at 35% CO conversion. Standard reaction conditions.

**Table 8**
Campbell's degree of rate control for non-equilibrated steps calculated at 25% CO conversion.

| Experimental Condition | $X_{RC,5}$ | $X_{RC,14}$ | $X_{RC,16}$ | $\sum X_{RC,i}$ |
|---|---|---|---|---|
| 1 | 0.786 | 0.036 | 0.0019 | 0.824 |
| 2 | 0.612 | 0.206 | 0.0006 | 0.818 |

Experimental condition: 2.7 bars, 473 K; Feed 1: 36.7% $H_2$, 16.7% $N_2$, 8% CO, 5.3% $CO_2$, 33.3% steam; Feed 2: 36.7% $H_2$, 16.7% $N_2$, 2.7% CO, 10.6% $CO_2$, 33.3% steam.

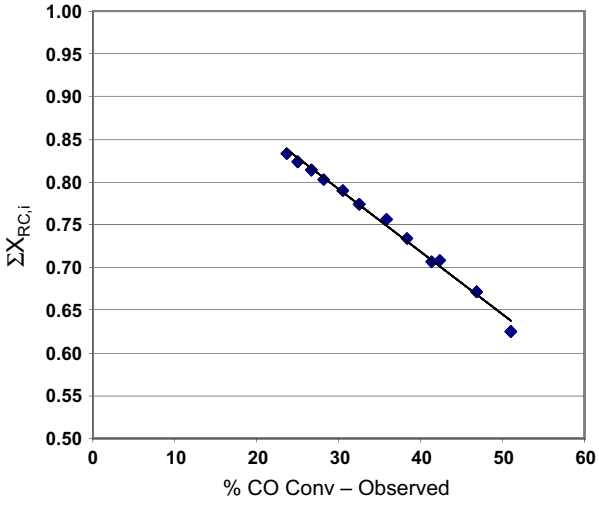


**Fig. 14.** Total Campbell's degree of rate control versus % CO conversion.

Such an analysis is conducted by adjusting the free energy of a specific surface intermediate, for example, by changing its binding energy, while keeping the free energies of all other surface intermediates constant, as well as constant energies for transition states. In our case, altering $BE_H$, $BE_{HCOO}$, and $BE_{OH}$ may change surface coverages, but the previously determined kinetic importance of individual reaction steps will remain unchanged, because conclusions from Campbell's degree of rate control are controlled by locations in energy of transition states, and not binding energies of reaction intermediates.

## 5. Discussion

The 8 step closed catalytic cycle given in Table 5 depicts the mechanism of the low temperature water gas shift reaction on copper. Hydrogen formation occurs by the dissociation of water and the recombination of surface hydrogen. Surface hydroxyl reacts with $CO^*$ to give a cis surface carboxyl intermediate that resides in equilibrium with its trans form. The latter species reacts with a surface hydroxyl to give carbon dioxide and water to complete the cycle. Our approach, to initially use 18 reaction steps, including formate reactions and reactions associated with the redox mechanism, allows us to avoid bias toward a certain mechanism. For example, the reaction of surface CO and OH leads to a carboxyl intermediate rather than a surface formate, since the latter reaction is energetically very demanding. Our model using the carboxyl mechanism describes all our data over a wide range of conditions and, more importantly, permits us to explain observations resulting from catalyst modifications. Thus, our study corroborates and amplifies the original work of Gokhale et al. [11].

All adsorption–desorption steps are in quasi-equilibrium. And although there is no single exergic step, the dissociation of water, with the ratio $\delta$ of 0.88, is the furthest from equilibrium (Table 5). This ratio is a good measure of the impact of a reaction step, in our case water dissociation, on the reaction rate, and agrees with the analysis using Campbell's degree of rate control. Interestingly, Campbell and Daube [5], while discussing the redox and formate-mediated mechanisms, showed that for either of these mechanisms, water dissociation would be the rate-determining step. The activation energy they developed for water dissociation from a surface science investigation on Cu (1 1 1) was 113 kJ/mol. The DFT-calculated value is 131 kJ/mol [11]. And our model, using the DFT value as an adjustable parameter, gave an activation energy of 125 kJ/mol, close to the experimental value of Campbell and Daube. Besides water dissociation, the reversible formation of the carboxyl intermediate, with $\delta$ equal to 0.54, is also non-equilibrated with an activation energy of 49 kJ/mol. Of all DFT-derived activation energies on Cu(1 1 1) [11] that we used, the values for these two reactions were the only activation energies that the model needed to adjust. This behavior plus the fact that the values of BE we used were either the same or very close to those calculated on Cu(1 1 1) [11] suggests that the Cu particles in Cu:ZnO:$Al_2O_3$ which are greater than 10 nm, behave like Cu(1 1 1). This observation is in accord with the experimentally derived conclusion of Campbell and Daube [5].

Interestingly, the endothermic desorption of dihydrogen with a high activation energy of 98 kJ/mol [11] and the corresponding dissociative adsorption is equilibrated; whereas, the reaction of $CO^*$ with $OH^*$ with $E_{f,14}$ of only 49 kJ/mol to form $COOH^*_{cis}$ is a non-equilibrated reversible step with possible kinetic significance. Indeed, as we change the inlet gas ratio so that CO is decreased from 8% to 2.7% and $CO_2$ is increased from 5.3% to 10.6%, the reaction rate decreases by ca. factor of 3 (Fig. 10). Concomitantly, $\delta$ for the water dissociation step decreases to 0.62 while that for the $COOH^*$ formation step increases to 0.8, indicating that this step is now more irreversible and, perhaps, more kinetically significant. We cite this example of change, because it shows that variations in reaction conditions can subtly alter the active surface which we observe, via our model, kinetically.

Under our conditions, increasing $CO_2$ levels by a factor of 2 in the feed does not increase HCOO**. Bidentate formate coverage is increased mainly by increasing pressure and decreasing temperature. Importantly, formate coverage is reduced significantly in the presence of alkali promoter. Kinetically, the model indicates a large reduction in $BE_{HCOO^{**}}$, implying an alkali-assisted destabilization of this intermediate.

A microkinetic model not only addresses important mechanistic questions, but also helps determine how to enhance kinetically significant steps of a catalytic cycle. The 4 catalysts in Table 7 are a case in point. All 4 catalysts show results similar to those given in Table 5, with Reactions 1–4 and 18 being in quasi-equilibrium, and with steam dissociation having the same degree of irreversibility of ca. 0.88 for all the catalysts. The only adjustable parameter that differentiates the kinetics for the catalysts is $BE_H$; thus steps containing H* are necessarily affected.

Reaction 2 is in quasi-equilibrium, and the equilibrium constant for Reaction 2, $K_{2,eq}$, increases with an increase in hydrogen binding energy concomitant with an increase in H*. However, the surface coverage of adsorbed H atoms remains low for all cases, and the increase in activity caused by changing $BE_H$ must be caused by another effect. In this respect, the value of $k_{i,for}$ for Reaction 5 increases (Fig. 15) as catalyst activity increases; with $BE_H$ influencing $K_{5,eq}$ as shown below

$$K_{5,eq} \propto \exp\left(\frac{-BE_H}{RT}\right) \tag{11}$$

But because this step is endothermic, the model was parameterized in terms of the reverse rate constant and the equilibrium constant:

$$k_{5,for} = k_{5,rev}K_{5,eq} \propto \exp\left(\frac{-BE_H}{RT}\right) \tag{12}$$

For the other non-equilibrated reaction steps, 14 and 16, the forward and reverse rate constants are the same for all 4 catalysts, indicating that formation and reaction of the carboxyl intermediate

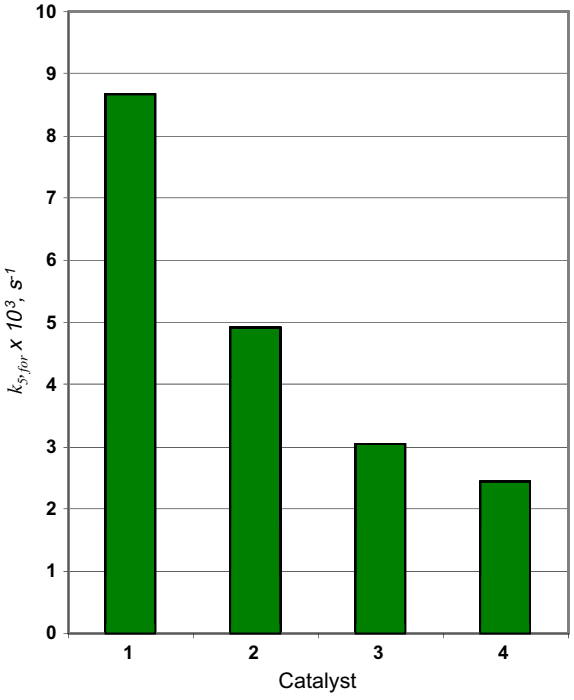


**Fig. 15.** Forward rate constant for water dissociation for Catalysts 1–4 (Table 7). Standard reaction conditions.

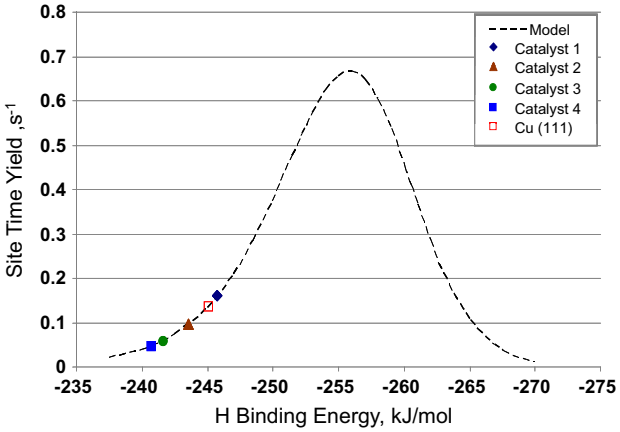


**Fig. 16.** Model derived volcano plot demonstrating effect of H binding energy on site time yield. Catalysts 1–4 (Table 7) and Cu(1 1 1) indicated on the plot. 30% CO conversion. Standard reaction conditions.

does not play as important a role for enhancing catalytic activity. This analysis demonstrates that facility in steam dissociation is important for high catalytic activity.

Importantly, the model allows us to ascertain to what extent site time yields can be increased. Using the model, we obtain site time yields at varying $BE_H$ while also changing total flow rates to ensure constant 30% CO conversion. This analysis results in a volcano plot (Fig. 16). The figure also includes model results for the 4 catalysts as well as for Cu(1 1 1), all at 30% conversion. As $BE_H$ increases to -256 kJ/mol, Y increases, but with further increase in $BE_H$, Y decreases: an excellent example of the Sabatier Principle. Catalyst 1 and 2 are prepared identically except for the calcination temperature, and their results bracket the result with Cu(1 1 1). This result agrees with the suggestion [32,33] that subtle but important chemical promotion by ZnO on Cu is possible. Yttrium oxide and $Nb_2O_3$ have a deleterious effect on the LTS rate, indicating that strong interaction of Cu with such oxides is possible, although, in this case, a negative one. Noting the work of Nakamura et al. [6], where they found the more open Cu(1 1 0) surface to be more active than Cu(1 1 1), we speculate that in order to achieve the maximum rate of Fig. 16, the Cu catalyst surface should be made to mimic Cu(1 1 0).

The value of $BE_H$, as noted from Eqs. (3) and (11), perturbs the activation barrier for steam dissociation, which is an endothermic step, by changing the enthalpy of formation of surface H. A similar perturbation of the activation barrier can also occur if we keep $BE_H$ constant and perturb the inherent activation energy of steam dissociation. In this case, as this activation barrier is decreased, the net rate will increase until its kinetic significance decreases relative to another step or diffusion limitations are reached.

## 6. Concluding Remarks

Eight elementary reactions that constitute a closed catalytic cycle adequately describe the mechanism of the water gas shift reaction on Cu. Adsorbed hydrogen atoms formed from the dissociation of water desorb as dihydrogen, while OH* reacts with surface CO to form a carboxyl intermediate which in turn reacts with another OH* to give $CO_2$. Besides these 8 reactions, two equilibrated reactions, which are not part of the LTS catalytic cycle, produce the observed bidentate formate species. This surface formate is a spectator species, and although it does not participate directly in the shift reaction, its high surface coverage, especially at high pressures and low temperatures, can influence the LTS reaction by blocking surface sites. This mechanistic description concurs with

the earlier work of Gokhale et al. [11]. Indeed, the robustness of our model is due in part to the use of DFT-calculated values for binding energies, activation energies, and preexponential factors we obtained from Ref. [11]. And although our model differs from previous models in the literature, several aspects of our work are in step with previous observations of, for example, Ovesen et al. [4] regarding formate being a spectator species, and Campbell and Daube [5] regarding the kinetic importance of the water dissociation step and the kinetic resemblance of Cu–ZnO–$Al_2O_3$ catalysts to Cu(1 1 1).

The kinetic significance of each reaction step was obtained by noting its degree of irreversibility ($\delta$) and by determining Campbell's degree of rate control. Both water dissociation and carboxyl formation have $\delta$ values approaching 1, and as conditions change, one or the other step becomes more kinetically significant. Complexity in the LTS surface chemistry arises due to possible changes in the binding energies of adsorbed components. For the catalysts and experimental conditions investigated here, we found the values of $BE_H$, $BE_{OH}$, and $BE_{HCOO}$, to be important, with $BE_H$ being the most sensitive. Under other conditions and with other Cu-based catalysts, binding energies and even activation energies may change to a greater extent; however, the mechanism and model we have described should hold.

## Acknowledgments

We thank the management at BASF Corporation for their support for carrying out this research. We gratefully acknowledge funding from the Department of Energy (Basic Energy Sciences) and BASF Corporation. We thank Dr. Ivan Petrovic, and Ms. Beth Nartowicz (BASF Corporation) for setting up the $N_2O$ chemisorption method, and Ms. Nartowicz also for carrying out all the chemisorption measurements. And finally, we thank Mr. David Disantis (BASF Corporation) for his assistance in obtaining kinetic data.

## References

[1] T.M. Yurieva, Kinet. Katal. 10 (1969) 862.
[2] D.C. Grenoble, M.M. Estadt, D.F. Ollis, J. Catal. 67 (1981) 90.
[3] C.V. Ovesen, P. Stoltze, J.K. Nørskov, C.T. Campbell, J. Catal. 134 (1992) 445.
[4] C.V. Ovesen, B.S. Clausen, B.S. Hammershøi, G. Steffensen, T. Askgaard, I. Chorkendorff, J.K. Nørskov, P.B. Rasmussen, P. Stoltze, P. Taylor, J. Catal. 158 (1996) 170.
[5] C.T. Campbell, K.A. Daube, J. Catal. 104 (1987) 109.
[6] J. Nakamura, J.M. Campbell, C.T. Campbell, J. Chem. Soc. Faraday Trans. 86 (1990) 2725.
[7] J. Yoshihara, S. Parker, A. Schafer, C.T. Campbell, Catal. Lett. 31 (1995) 313.
[8] N.A. Koryabkina, A.A. Phatak, W.F. Ruettinger, R.J. Farrauto, F.H. Ribeiro, J. Catal. 217 (2003) 233.
[9] P. Liu, J.A. Rodriguez, J. Chem. Phys. 126 (2007) 164705.
[10] J.L.C. Fajin, M.N.D.S. Cordeiro, F. Illas, J.R.B. Gomes, J. Catal. 268 (2009) 131.
[11] A.A. Gokhale, J.A. Dumesic, M. Mavrikakis, J. Am. Chem. Soc. 130 (2008) 1402.
[12] T. van Herwijnen, W. A de Jong, J. Catal. 63 (1980) 83.
[13] T. van Herwijnen, W. A de Jong, J. Catal. 63 (1980) 94.
[14] J.A. Dumesic, D.F. Rudd, L.M. Aparicio, J.E. Rekoske, A.A. Treviño, The Microkinetics of Heterogeneous Catalysis, American Chemical Society, Washington, DC, 1993.
[15] F. Schüth, K. Unger, in: G. Ertl, H. Knözinger, J. Weitkamp (Eds.), Handbook of Heterogeneous Catalysis, vol. 1, 1997, p. 72.
[16] J.-L. Li, T. Inui, Appl. Catal. A 137 (1996) 105.
[17] R.E. Reitmeier, H.W. Fleming, US Patent 3,388,972 (1968) (to Catalysts and Chemicals Inc.).
[18] Y. Cai, S. Davies, J. Wagner, US Patent 6,627,572 B1 (2003) (to Süd-Chemie Inc.).
[19] L. Lloyd, D.E. Ridler, M.V. Twigg, in: M.V. Twigg (Ed.), Catalyst Handbook, second ed., Wolfe Publishing Ltd., England, 1989.
[20] G.C. Chinchen, C.M. Hay, H.D. Vandervell, K.C. Waugh, J. Catal. 103 (1987) 79.
[21] S. Kandoi, J. Greeley, M.A. Sanchez-Castillo, S.T. Evans, A.A. Gokhale, J.A. Dumesic, M. Mavrikakis, Topics Catal. 37 (2006) 17.
[22] M.A. Sanchez-Castillo, R.J. Madon, J.A. Dumesic, J. Phys. Chem. 109 (2005) 2164.
[23] I. Chorkendorff, J.W. Niemantsverdriet, Concepts of Modern Catalysis and Kinetics, Wiley-VCH GmbH & Co. KGaA, Weinheim, 2003.
[24] M. Caracotsios, Athena Visual Studio, www.athenavisual.com.
[25] R.J. Madon, M. Boudart, I&EC Fundamentals 21 (1982) 438.
[26] M.A. Vannice, Kinetics of Catalytic Reactions, Springer, 2005, p. 77.
[27] M. Boudart, Topics Catal. 14 (2001) 181.
[28] Y. Yang, C.A. Mims, R.S. Disselkamp, C.H.F. Peden, C.T. Campbell, Topics Catal. 52 (2009) 1440.
[29] K. Gründler, M. Irgang, N. Neth, M.J. Sprague, G. Zirker, European Patent 0 205 130 B1 (1992) (to BASF).
[30] C.T. Campbell, Topics Catal. 1 (1994) 353.
[31] C. Stegelmann, A. Andreasen, C.T. Campbell, J. Am. Chem. Soc. 131 (2009) 8077.
[32] N.-Y. Topsøe, H. Topsøe, J. Mol. Catal. A 141 (1999) 95.
[33] P. L Hansen, J.B. Wagner, S. Helveg, J.R. Rostrup-Nielsen, B.S. Clausen, H. Topsøe, Science 295 (2002) 2053.